KECK DEEP FIELDS. I. OBSERVATIONS, REDUCTIONS, AND THE SELECTION OF FAINT STAR-FORMING GALAXIES AT REDSHIFTS $z\sim$4, 3, AND 2 [1]

Marcin Sawicki[2]
Dominion Astrophysical Observatory, Herzberg Institute of Astrophysics, National Research Council, 5071 West Saanich Road, Victoria, B.C., V9E 2E7, Canada; and Caltech Optical Observatories, California Institute of Technology, MS 320-47, Pasadena, CA 91125, USA

David Thompson
Caltech Optical Observatories, California Institute of Technology, MS 320-47, Pasadena, CA 91125, USA
Accepted for publication in ApJ

ABSTRACT

We introduce a very deep, $\mathcal{R}_{lim}\sim$27, multicolor imaging survey of very faint star-forming galaxies at $z\sim$4, $z\sim$3, $z\sim$2.2, and $z\sim$1.7. This survey, carried out on the Keck I telescope, uses the very same $U_nG\mathcal{R}I$ filter system that is employed by the Steidel team to select galaxies at these redshifts, and thus allows us to construct identically-selected, but much fainter, samples. However, our survey reaches $\sim$1.5 mag deeper than the work of Steidel and his group, letting us probe substantially below the characteristic luminosity L^* and thus study the properties and redshift evolution of the *faint* component of the high-z galaxy population. The survey covers 169 arcmin^2 in three spatially independent patches on the sky and — to $\mathcal{R}{\leq}27$ — contains 427 $G\mathcal{R}I$-selected $z\sim$4 Lyman Break Galaxies, 1481 $U_nG\mathcal{R}$-selected $z\sim$3 Lyman Break Galaxies, 2417 $U_nG\mathcal{R}$-selected $z\sim$2.2 star-forming galaxies, and 2043 $U_nG\mathcal{R}$-selected $z\sim$1.7 star-forming galaxies. In this paper, the first in a series, we introduce the survey, describe our observing and data reduction strategies, and outline the selection of our $z\sim$4, $z\sim$3, $z\sim$2.2, and $z\sim$1.7 samples.

Subject headings: cosmology: observations — galaxies: evolution — galaxies: high-redshift — galaxies: starburst — galaxies: statistics

1. INTRODUCTION

By $z\sim$1, when the Universe was about half its current age, many of the properties of the present-day galaxy population were already in place. Although the rate of star formation in the Universe as a whole was an order of magnitude higher at $z\sim$1 than it is today (Lilly et al. 1996), there already existed a well-developed luminosity function of quiescent galaxies (Lilly et al. 1995) as well as an established population of galactic bulges and disks (Schade et al. 1995, Brinchman et al. 1998) with normal-looking Tully-Fisher rotation curves (Vogt et al. 1997). Thus, while clearly much remains to be learned about galaxies and galaxy evolution at $z<$1, we must look to higher redshifts, $z>$1, to witness many of the key events in the story of galaxy formation.

To efficiently reach beyond $z>$1 requires techniques that let us robustly select high-z galaxies, preferably with some — even crude — redshift information, while minimizing contamination by the far more numerous foreground objects. Such selection is possible using multi-color broadband photometry that is sensitive to the imprint on galaxy spectra of coarse spectral features such as the Lyman break at rest-912Å, the Balmer and 4000Å breaks at 3648–4000Å, and — in the rest-frame infrared

— the H$^-$ opacity bump at 1.6μm (e.g., Sawicki 2002). One such multicolor approach is the technique of photometric redshifts in which the most likely redshift of an object is estimated by comparing its observed and predicted broadband spectral energy distributions (e.g., Connolly et al. 1995; Sawicki, Lin, & Yee 1997; Bolzonella et al. 2000; Sawicki 2002; Csabai et al. 2003). Another, even simpler, technique — popularized and shown to be very effective through extensive spectroscopic follow-up by Steidel and collaborators (e.g., Steidel et al. 1996, 1999, 2003) — straightforwardly selects high-z star-forming galaxies by their distinctive colors in an optical color-color diagram. Extensive spectroscopic follow-up of such color-color selected Lyman Break Galaxies (LBGs) has allowed Steidel and his collaborators to amass very large samples of $\sim$10^3 *spectroscopically confirmed* galaxies at $z\sim$3 (selection in the $U_n - G$ vs. $G - \mathcal{R}$ color space) and $z\sim$4 (selection in the $G - \mathcal{R}$ vs. $\mathcal{R} - I$ space) while a recent extension of the technique to lower redshifts ($z\sim$1.7, $z\sim$2.2; Erb et al. 2003, Steidel et al. 2004) has also started to yield promising results.

The imaging samples assembled by the Steidel team are designed for efficient spectroscopic confirmation and, therefore, are limited to relatively bright objects ($\mathcal{R}{\lesssim}$25.5 or $I{\lesssim}$25). Consequently, they do not probe significantly fainter than the characteristic luminosity, L^*, at which the galaxy luminosity function changes slope.

The transition at L^* in the galaxy luminosity function is likely an imprint of how galaxies form and evolve and the comparison of galaxies above and below L^* may tell us much about what different processes are responsible for this evolution. The mass function of dark matter

halos, predicted from simulations of dark-matter clustering (e.g., Jenkins et al. 2001), is essentially a power law on mass scales that encompass the range of galaxy masses; in contrast, the observed luminosity function of galaxies, both at low redshift and high, exhibits different behaviours above and below a characteristic luminosity, L^*. This different shape in the luminisity function suggests that different mechanisms dominate the evolution of galaxies above and below L^* and that therefore our understanding of galaxy formation and evolution may profit from studying the evolution of not just the bright end but also the faint component of the galaxy population at high redshift. Similarly, because the strength of the clustering of dark matter halos depends on the halo mass, a careful study of galaxy clustering properties as a function of both epoch *and* galaxy luminosity may inform us about how the properties of dark matter halos affect the star formation that occurs in the galaxies that they host.

Motivated by the twin goals of studying the dependence of the galaxy luminosity function and of galaxy clustering on epoch *and* luminosity, we have carried out a very deep ($\mathcal{R}_{lim} \sim 27$), wide-area (169 arcmin^2), multi-color ($U_n G \mathcal{R} I$) *imaging* survey of galaxies that are significantly fainter than those reached in the well-known studies by the Steidel team. Our survey uses the *same* $U_n G \mathcal{R} I$ filter system that is used by Steidel and his collaborators for selecting their $z \sim 4$, $z \sim 3$, $z \sim 2.2.$, and $z \sim 1.7$ samples, but probes significantly fainter — up to 1.5 magnitudes, or a factor of 4 in luminosity. Spectroscopic follow-up of their color-color selected samples has allowed Steidel et al. (1999, 2003, 2004) to precisely characterize important quantities, including selection volumes and fractions of low-z interlopers. Our use of identical filters and color-color selection permits us to apply this knowledge in a relatively straightforward way to our samples. Thus, even without what — at the magnitudes of the objects in our survey — would have been *very* expensive spectroscopy, we can understand and correct for the selection effects that are at play.

In the present paper — which serves as the introduction to our survey — we describe our observations (§ 2) and data reductions (§ 3), including an assessment of the photometric completeness and surface brightness selection. We then outline the photometric selection of our $z \sim 4$, $z \sim 3$, $z \sim 2.2$, and $z \sim 1.7$ galaxy samples (§ 4) and compare and contrast our survey with other deep imaging surveys (§ 5). Subsequent papers in this series will study the faint end of the high-z galaxy luminosity function and the clustering of faint galaxies at high redshift and will extend this work into the near-IR.

Unless specifically stated otherwise, throughout this series of papers we normalize fluxes on the AB magnitude system (Oke 1974) and adopt $\Omega_M = 0.3$, $\Omega_\Lambda = 0.7$, and $H_0 = 70$ km s^{-1} Mpc^{-1}.

2. SURVEY STRATEGY AND OBSERVATIONS

The design of the survey reflects our goal of robustly studying the evolution of the *faint* (sub-L^*) component of the star-forming galaxy population at high redshift. Briefly:

- To reach *deep* into the sub-L^* population we carried out very deep imaging using the LRIS imaging spectrograph on the 10m Keck I telescope.

- To *robustly* identify high-z star-forming galaxies and to ensure a smooth joining with the Steidel et al. work at brighter magnitudes, we used the very same filter set and selection techniques as are used in their larger, but shallower, spectroscopically-calibrated surveys.

- To avoid being dominated by small number statistics *and* by cosmic variance the survey covers a large area (169 arcmin^2) that is split into three spatially-independent patches.

We call our survey the Keck Deep Fields (KDF).

The $G \mathcal{R} I$ color composite images shown in Figure 1 give a visual overview of the KDF, while Table 1 summarizes key information about our survey fields, including field coordinates and sizes, foreground extinction, exposure times per filter, image quality, and limiting depth. As shown in Fig. 1, the survey consists of five LRIS fields, two pairs of which are abutting along their long edges. The survey area is thus split into two larger 'patches' of two LRIS fields each and a third, smaller patch that consists of a single LRIS field. Our field-naming convention is based on the right ascensions of the patches and we call the five fields 02A, 03A and 03B (together comprising the 03 patch), and 09A and 09A (the 09 patch). The three patches are widely separated on the sky, helping to ensure that the effects of large-scale structures are averaged out. The purpose of abutting pairs of fields into the larger patches is to give us improved ability to study galaxy clustering (Sawicki & Thompson, in preparation), where the larger *contiguous* area is important as it gives us many more baselines in general and, particularly, many long baselines few of which are available in a single LRIS field. Our 09 patch partially overlaps one of the $U_n G \mathcal{R} I$ fields (field Q0933+289) from the survey of Steidel et al. (2003); this patch contains a $z=3.43$ quasar (the brightest object in the 09A field — see Figure 1), but we do not expect its presence to bias our science as there is no evidence of a galaxy overdensity at the QSO redshift in the extensive Steidel et al. (2003) spectroscopy of this field.

Our survey was carried out in dark-time over two three-night observing runs: 2001 December 18–20 UT (hearfter Run 1) and 2002 December 2–4 UT (hereafter Run 2). All data were taken using the LRIS imaging spectrograph (Oke et al. 1995; McCarthy et al. 1998; Steidel et al. 2003) mounted on the Keck I telescope. LRIS provides two independent channels, fed through a dichroic beamsplitter, which *simultaneously* observe two separate wavelength ranges. We used the D560 dichroic, which allowed us to observe simultaneously in U_n (or G) on the blue side and $\mathcal{R}$ (or I or Z) on the red side. The red channel uses a SITe/Tektronix 2048×2048 pixel, backside-illuminated CCD with 0.215$''$ pixels and a quantum efficiency that peaks at 70% at 6000Å and remains above 50% to 8500Å. The detectors in the blue channel changed half-way through the project: during Run 1 we had to use a fairly average SITe 2048×2048 pixel CCD (QE$\sim$35% at U_n and $\sim$65% at G), but during Run 2 we benefited from an excellent mosaic of two UV-optimized EEV (Marconi) 2048×4096 pixel CCDs with 0.135$''$ pixels and very high UV and blue quantum efficiency (QE$>$60% at U_n and $>$85% at G). In all these detectors dark current was negligible.

We lost the bulk of the first night of Run 1 to weather and instrument problems, but the remaining two nights of Run 1, as well as all three nights of Run 2 were both photometric and trouble-free. $\mathcal{R}$-band seeing ranged over 0.7–$1.4''$, although we rejected the frames with the poorest image quality when making our stacked images (§ 3). During part of one night of Run 1 the seeing was particularly poor, affecting all the G-band images of one of the fields (field 03A). Consequently, all the Run 1 G-band images of this field was rejected and was redone in Run 2 while at the same time some additional I-band imaging of that field was simultaneously obtained using the red channel of the instrument.

The data were acquired as a series of short, dithered exposures. The U_n-band frames were always acquired simultaneously with the $\mathcal{R}$-band frames, and the G-band frames with the I-band ones. Aditionally, a small amount of Z-band data, taken through the long-pass RG850 filter, were taken in parallel with the U_n-band observations; these Z-band data will be presented elsewhere. Individual exposure times were 1200s in U_n-band, 1200s in G-band, 525s (or 585s) in $\mathcal{R}$-band, and 325s (or 360s) in I-band. Exposure times in the red channel ($\mathcal{R}$ and I bands) — where the night-time sky is quite bright even during darktime — were short to avoid straying into the non-linear regime of the CCD response.

We wished to dither but did not want to waste time not taking data in one channel while waiting for the other channel to finish. Consequently, we set the red channel exposure times so that the end of the last read-out of a set of red exposures coincided with the end of the read out of a blue exposure:

$$N_{exp}^{red} \times (t_{exp}^{red} + t_{read}^{red}) = (t_{exp}^{blue} + t_{read}^{blue}), \qquad (1)$$

where t_{exp} are the exposure times, t_{read} are the readout times, and N_{exp}^{red} is the number of red channel exposures taken during one blue-channel exposure (N_{exp}^{red}=2 for $\mathcal{R}$-band and 3 for I-band). After each such exposure sequence consisting of one blue-channel and N_{exp}^{red} red-channel exposures, the telescope was offset following a quasi-random pattern on a nine-point square grid with $24''$ or $30''$ edges. This dithering was done to allow the subsequent exclusion of bad pixels from the stacked frames and to permit the masking-out of sources in the construction of flat-field images and fringe frames from the imaging data.

In total, our good $U_nG\mathcal{R}I$ images of the five fields consumed 71.1 hours of *exposure time*. This number does not include overheads, images that were excluded from the final stacks because of poor image quality etc., nor the Z-band data. Once processed and stacked, these images comprise some of the deepest multiwavelength imaging taken, particularly the U-band, over this wide an area.

3. DATA REDUCTION

3.1. *Pre-processing and frame stacking*

The data were processed in IRAF[3] using a fairly standard algorithm for processing CCD data. The primary

deviation is embodied in the iterative determination of the fringe-correction image and the corrected domeflat. We reduced each dataset from a different CCD separately and, where possible, we also independently processed data from separate nights.

In particular, the initial processing of the data consisted of first subtracting the bias signal from each image using the overscan regions. Separate bias frames were then stacked and subtracted from the science data to correct for any residual bias structure. We then constructed normalized domeflats in each filter, rescaling the images to a constant mean value and stacking them with sigma-clipping to remove cosmic rays. We constructed a bad pixel mask from the bias and domeflat images, marking as bad any hot or dead pixels and bad columns or charge traps.

After this initial preparation, we flatfielded the science data with the domeflats, then rescaled and stacked the images to reject real sources on the sky. We used these stacked images to construct a fringe frame for the G, $\mathcal{R}$, and I data (the U_n data did not need fringe correction). Any residual gradients were used to correct the domeflats, and these few steps repeated until we converged on a good fringe frame and corrected domeflat. The final reduction of the science data produced individual flat-fielded, fringe-corrected images with zero mean sky values.

We then shifted the images (using integer pixle shifts) to correct for dithering offsets and stacked all of the data for each field and filter combination to produce preliminary deep images. The deep images were chopped, scaled, and convolved as necessary to subtract from the individual images to aid in identifying and masking satellite or meteor trails, asteroids, and cosmic rays. Instrumental magnitudes for a set of isolated, unsaturated sources in common to all frames were determined and used to multiplicatively rescale the images to constant photometry. We measured the sky noise (σ_i) and full-width at half-maximum ($FWHM_i$) of the seeing in each of these images, i, and then produced the final deep image with a modified variance weighting, which is corrected for the seeing:

$$weight_i \propto 1/(\sigma_i^2 FWHM_i). \qquad (2)$$

This scheme gives higher weight to the images with the best seeing and/or the lowest noise, resulting in a gain in the depth of the final, stacked images.

3.2. *Image registration, trimming, and photometric calibration*

Next, the stacked U_n, G, and I images were geometrically transformed to match their corresponding $\mathcal{R}$-band images using the positions of multiple bright point sources. These aligned $U_nG\mathcal{R}I$ images of each field were then trimmed to exclude areas of low S/N around the edges that were a byproduct of spatial dithering; this trimming was done so that in each field the trimmed images in each of the four bands covered only a common area, with all low-S/N edge areas trimmed out. Even after this trimming, sufficient overlap remained between the 09A and 09B images (5.0 arcmin^2) and the 03A and 03B images (1.8 arcmin^2) to allow us to later accurately tie together the two fields of each patch.

The images were then photometrically calibrated. We tied our photometric system to photometrically calibrated deep U_nGRI images that were kindly provided to us for that purpose by Chuck Steidel. Although the filter sets used in Steidel's images and in ours were nearly identical, we nevertheless computed the invariably small color terms in our photometric transformations since we wanted to be able to replicate without bias the Steidel et al. (1998, 2003, 2004) color-color selection of high-z galaxies. The use of these color terms, derived from the comparison of images obtained using our apparatus with those taken by Steidel et al. in their surveys, ensures that any wavelength-dependent differences due to detector QE, mirror reflectivity, etc., are calibrated out, and that we are working on the same photometric system as Steidel et al. are. As the final step in our photometric calibration, we have corrected for the very small effect of foreground Galactic dust extinction as determined from the Schlegel, Finkbeiner, & Davis (1998) dust maps. The $E(B-V)$ values of these dust corrections are given in Table 1.

In addition to the natural-seeing images, we also produced seeing-matched U_nGRI images for each field. These seeing-matched images were made for use in measuring object colors (§ 3.3) and were made by smoothing the three images of the field that have better seeing to match the seeing in the fourth, poorest-quality image. The smoothing was done using a Gaussian kernel whose width was determined for each image based on the sizes of multiple bright but unsaturated point sources. The FWHM sizes of the seeing in the resultant smoothed images are given as "common smoothed seeing" in Table 1). They are typically FWHM $\sim$1.0–1.1″, except for the 03A field for which the final image quality was significantly worse at 1.4″. Our $\sim 1''$ seeing is very comparable to the seeing in the shallower U_nGRI surveys of Steidel et al. (1999, 2003, 2004).

3.3. *Object detection and photometry*

Overall, our photometric approach is very similar to that used by Steidel and collaborators, including the use of the same U_nGRI filter set, $\mathcal{R}$-band detection of objects, and color measurement through circular apertures. The specifics are discussed below and any differences in approach are noted.

Ideally, we would have wished to *detect* galaxies at a constant *rest-frame* wavelength irrespective of redshift. Given our data and redshift ranges of interest this could have been done at $\lambda \approx 1700$Å which corresponds to observed I-band at $z\sim4$, $\mathcal{R}$-band at $z\sim3$, and G-band at $z\sim2$. However, because our $\mathcal{R}$-band images are extremely deep, we chose to do object detecion in the $\mathcal{R}$-band images only. This approach is completely analogous to the procedure used by the Steidel team and has the virtue of simplicity in that it results in only one source catalog per field. Given the depth of our $\mathcal{R}$-band images and the relatively mild $\mathcal{R} - I$ and $G - \mathcal{R}$ colors of $z\sim4$ and $z\sim2$ galaxies, respectively (see Figs. 4 and 5, and also Steidel et al. 1998, 2003, 2004), our $\mathcal{R}$-band object detection should not bias our samples in any significant way.

We used the SExtractor package (Bertin & Arnouts, 1996) for object detection and photometry. To detect objects, we ran SExtractor on the *unsmoothed $\mathcal{R}$*-band images. Total $\mathcal{R}$-band magnitudes are SExtractor's MAG_AUTO apertures which are Kron-like (Kron 1980) elliptical apertures in which fluxes are corrected for any contaminating close companions through masking and image symmetrization. Colors were measured in Sextractor's dual image mode, using the unsmoothed images for object detection and the smoothed, seeing-matched images for color photometry. In keeping with the approach of the Steidel team, we used 2.0″-diameter circular apertures (Steidel et al. 2003) for color measurement. Finally, the instrumental magnitudes were transformed onto the AB system (Oke 1974) using the zeropoints and color terms determined in § 3.2. The total magnitudes in the U_n, G, and I bands were then straightforwardly computed from the $\mathcal{R}$-band total magnitudes and aperture colors via

$$m_{tot} = \mathcal{R}_{tot} - (\mathcal{R}_{ap} - m_{ap}), \qquad (3)$$

where $\mathcal{R}$ is the $\mathcal{R}$-band magnitude, m represents the magnitude in one of the other bands (U_n, G, or I) and the subscripts ap and tot denote aperture and total magnitudes, respectively.

Our treatment of "drop-out" objects also follows closely the approach of Steidel et al. (2003). If an object's reported flux in the U_n (or G) band is greater than the 1σ fluctuation in the sky background over the size of our color aperture then the object is considered detected in that band and is assigned an aperture magnitude that corresponds to that measured flux. If, on the other hand, the reported flux is below the 1σ threshold, the object is considered a drop-out and is assigned an upper flux limit that is defined as the magnitude that corresponds to the 1σ sky fluctuation.

The main difference between our procedure and that of Steidel and his team is that whereas they use an in-house modified version of FOCAS for object detection and photometry, we use SExtractor. The use of these two different programs has two potential consequences.

1. The first of these potential consequences is that the number of objects detected by SExtractor and FOCAS may be different as the two programs use different object-detection algorithms. If these were the case than we might expect a different number density of galaxies in the two surveys. However, this is *not* the case here: Table 1 lists the number densities of objects with $\mathcal{R}$=22.5–25.0 in our fields. These number densities are entirely consistent with the distribution of identically defined object densities in the 17 fields of Steidel et al. (2003) and the average of our five fields, <N>=27.7±2.9, is fully consistent with their 17-field average of <N>=25.9±1.9. We therefore conclude that any differences in object-finding between FOCAS and SExtractor are likely not significant for our purposes and result in variations that are certainly smaller than field-to-field scatter due to cosmic variance.

2. The second potential consequence of using SExtractor instead of FOCAS is that total fluxes measured by SExtractor may differ from those measured by FOCAS. Such difference may arise because the two programs use different ways of sky

estimation and different definitions of total aperture (SExtractor uses Kron-like apertures corrected for near neighbor contamination, whereas FOCAS uses simple padded isophotal magnitudes). However, given the small angular sizes of distant galaxies, the differences between FOCAS and SExtractor should be small — on order a few percent. Moreover, any strong differences would also also reflect in a discrepancy in the number density of $22.5 \leq \mathcal{R} \leq 25$ objects, and — as we discussed above — no such discrepancy is seen. Finally, in the most sensitive respect — that of determining object *colors* — we follow a recipe identical to that of Steidel and his team, measuring colors through fixed, $2''$-diameter apertures.

Overall, our object selection procedure and photometry are thus very similar to those used by Steidel et al. and we expect there to be no significant systematic differences between the two approaches.

The spatial distribution of $23 \leq \mathcal{R} \leq 27$ objects in our survey is shown in Fig. 2. Our catalog is clearly missing objects in the vicinity of very bright stars (c.f. Fig. 1), where SExtractor has trouble finding faint sources in the bright glow from the stars. However, these areas of low sensitivity are small and we will account for as needed using simulations (§ 3.4; also Sawicki & Thompson 2004). In all, our catalog contains 14579 objects with $23 \leq \mathcal{R} \leq 27$ in the 169 arcmin^2 of our survey.

3.4. *Depth, Completeness, and Surface Brightness Selection Effects*

We assess the depth of the Keck Deep Fields in two ways: by measuring the sky noise of our images and by conducting Monte Carlo simulations that seek to detect artificial objects implanted into the images.

Table 1 lists the sky surface brightness limits measured from pixel-to-pixel RMS fluctuation in several representative, object-free areas of each image. In the redder bands the image depth correlates closely with total exposure time, while in the bluer bands it has a pronounced dependence on run-to-run changes in detector sensitivity and on the sky brightness changes in the individual exposures that were coadded into the stacked images. In the four fields that received close to the full intended exposure time (fields 03A, 03B, 09A, and 09B) characteristic 1σ sky surface brightness limits are $\mu_{lim} \sim$ 30.7, 30.8, 30.0, and 29.4 mag/arcmin^2 in $U_n G \mathcal{R} I$. They are ~ 0.5 mag shallower in the 02A field. In contrast, the typical sky surface brightness limits of the imaging used by the Steidel team are 28.7, 29.0, 28.4, and 28.0 in $U_n G \mathcal{R} I$ (Steidel et al. 2003, 1999). Thus, over the bulk of our survey, we reach ~ 1.5–2 mag deeper in sky noise than do Steidel et al. Even in our relatively shallow 02A field we reach sky surface brightness limits that are 0.7–1.8 mag deeper than those in the Steidel et al. surveys.

Sky surface brightness limits are of course only part of what affects the sensitivity of faint object imaging. A second key ingredient is image quality, which is primarily influenced by seeing and is parametrized by the amplitude of the stellar FWHM. With the exception of the 03A field, typical seeing of our stacked images is $\sim 1''$, which is very comparable to the seeing in the data used by the Steidel team (Steidel et al. 2003).

We use Monte Carlo simulations to assess the combined impact of both seeing *and* sky surface brightness on our data. By their nature these simulations also take into account other effects that impact the detection rate, such as the poorer detection sensitivity around bright stars and the confusion by close companions. At this stage, we are only interested in simply determining the *detection* efficiency of faint objects in the $\mathcal{R}$-band KDF images and do not attempt here to ascertain the incompleteness of our LBG sample due to scatter out of color-color selection regions by photometric errors in object colors. Such more comprehensive simulations are part of our study of the LBG luminosity functions (Sawicki & Thompson, in prep.).

To gauge our detection efficiency, we made simulations that implanted artificial objects with a range of fluxes and sizes at random position into our images and which then attempted to recover them using the same procedures as those we used in § 3.3 to construct our source catalogs. To assess the sensitivity of our catalog to object surface brightness, we simulated a range of Gaussian-shaped sources with FWHM=0.5–2$''$. However, we note that HST imaging of LBGs shows them to be very compact, with half-light radii $r_{1/2} \sim 0.1$–0.3$''$ over a range of epochs: $z \sim 5$, $z \sim 3$, and $z \sim 2$ (Bremmer et al. 2004; Giavalisco, Steidel, & Macchetto 1996; Erb et al. 2003). Consequently, given that our catalog is based on ground-based $\mathcal{R}$-band images with FWHM$\geq 0.8''$, our target high-z galaxies are essentially unresolved point sources with FWHM that corresponds to the seeing.

The contours in Fig. 3 show the results of our detection-rate simulations. The fraction of objects recovered as a function of object FWHM and $\mathcal{R}$-band magnitude is shown for each of the five fields. As expected, the detection efficiency drops with increasing total magnitude and FWHM. The horizontal line in each panel shows the stellar FHWM as measured from several bright but unsaturated stars in the images and correspond to the "seeing ($\mathcal{R}$)" values in Table 1. As noted above, because of the very small sizes ($r_{1/2} \sim 0.2''$) of distant star-forming galaxies, the horizontal line also reasonably represents the expected FHWM of our targets. As a measure of the detection depth of our images we adopt the magnitude at which 50% of unresolved objects are detected (hereafter, $\mathcal{R}_{lim}$). These limiting detection magnitudes range over $\mathcal{R}_{lim}$=26.7–27.3 and are listed in Table 1 and shown as vertical lines in Fig. 3.

Overall, three of our five fields (03B, 09A, and 09B) reach object detection limits $\mathcal{R}_{lim} \sim 27.2$. The other two fields, 02A and 03A, reach $\mathcal{R}_{lim} \sim 26.7$. The ~ 0.5 mag difference in depth arises because the two shallower fields either had a shorter exposure time (02A) or poorer seeing (03A) than the three deeper fields.

In summary, the detection limits, $\mathcal{R}_{lim}$, tell us to what depth we can reasonably push our source list before encountering significant detection incompleteness. We find that $\mathcal{R}_{lim} \sim 27.0$ in the KDF, which is ~ 1.5 magnitudes deeper than the work of the Steidel team. The sky surface brightness limits that were discussed earlier tell us how deep we can push our matched-aperture color measurements without incurring photometric errors that are larger than those in the surveys of Steidel et al. Here, we also found that we can do so to ~ 1.5 magnitudes deeper

than is the case in the data of the Steidel team. Thus, overall, our U_nGRI survey can select galaxies in a manner that's identical to that used for the spectroscopically-calibrated selection of high-z star-forming galaxies by the Steidel group, but can do so with confidence for objects that are up to $\sim$1.5 magnitudes fainter, namely to $\mathcal{R}\sim$27.0. It is to the selection of high-z star-forming galaxies that we now turn.

4. PHOTOMETRIC SELECTION OF HIGH-Z GALAXIES

4.1. *Color-color selection criteria*

Steidel et al. (1999; 2003; 2004) have developed and extensively tested color-color selection criteria that efficiently and robustly select galaxies at $z\sim$4, $z\sim$3, $z\sim$2.2, and $z\sim$1.7. These selection criteria have evolved somewhat over time (c.f., e.g., Steidel et al. 1996, Erb et al. 2003) and in our work we use the most recent published selection criteria, which are as follows.

To select $z\sim$4 objects we use (Steidel et al. 1999)

$$\begin{aligned} G - \mathcal{R} &\geq 2.0, \\ G - \mathcal{R} &\geq 2(\mathcal{R} - I) + 1.5, \\ \mathcal{R} - I &\leq 0.6, \end{aligned} \tag{4}$$

for $z\sim$3 objects we use (Steidel et al. 2003)

$$\begin{aligned} G - \mathcal{R} &\leq 1.2, \\ U_n - G &\geq G - \mathcal{R} + 1.0, \\ G - \mathcal{R} &\geq -0.1, \end{aligned} \tag{5}$$

for $z\sim$2.2 objects we use (see Steidel et al. 2004)

$$\begin{aligned} G - \mathcal{R} &\geq -0.2, \\ U_n - G &\geq G - \mathcal{R} + 0.2, \\ G - \mathcal{R} &\leq 0.2(U_n - G) + 0.4, \\ U_n - G &\leq G - \mathcal{R} + 1.0, \end{aligned} \tag{6}$$

and for $z\sim$1.7 objects we use (Steidel et al. 2004)

$$\begin{aligned} G - \mathcal{R} &\geq -0.2, \\ U_n - G &\geq G - \mathcal{R} - 0.1, \\ G - \mathcal{R} &\leq 0.2(U_n - G) + 0.4, \\ U_n - G &\leq G - \mathcal{R} + 0.2. \end{aligned} \tag{7}$$

Additionally, we impose a faint magnitude limit of $\mathcal{R}\leq$27.0 motivated by the depth of our images. To guard against bright foreground interlopers we also impose a bright-end cut of $\mathcal{R}\geq$23.0.

The color-color selection criteria of Equations 4–7 are illustrated in the left-hand panels of Figures 4 and 5. The left panel of Figure 4 shows the region in $G-\mathcal{R}$ vs. $\mathcal{R}-I$ color space used to select galaxies at $z\sim$4 (Eq. 4). The left panel of Figure 5 shows in green, blue, and magenta the regions of U_n-G vs. $G-\mathcal{R}$ color-color space defined by Equations 5, 6, and 7 ($z\sim$3, 2.2, and 1.7), respectively.

The criteria of Eq. 5 correspond exactly to the union of LBG types C, D, M, and MD of Steidel et al. (2003); those of Equations 6 and 7, respectively, to what Steidel et al. (2004) call types BX and BM. In our work we do not use this nomenclature of Steidel et al., but — motivated by the observed redshift distributions (see below) of objects selected by Equations 4–7 — refer to them as the "$z\sim$4", "$z\sim$3", "$z\sim$2.2", and "$z\sim$1.7" criteria.

Extensive spectroscopy of hundreds of objects (Steidel et al. 1999, 2003, 2004) has shown that the redshift distributions of objects selected by the criteria of Equations 4–7 are — at least for their shallower samples — roughly Gaussian-shaped with $<z>$=4.13$\pm$0.26, $<z>$=2.96$\pm$0.26, $<z>$=2.20$\pm$0.32, and $<z>$=1.70$\pm$0.34. Spectroscopy has also shown that there is only small contamination by Galactic stars, low-z galaxies, or high-z AGN. At intermediate magnitudes, $\mathcal{R}\sim$24–25.5, the contamination by foreground interlopers — defined as objects with $z<1$ — is less than $\sim$5% in all three $U_nG\mathcal{R}$-selected redshift bins ($z\sim$1.7, 2.2, and 3; Steidel et al. 2003, 2004) and is likely to be even smaller in our samples because the ratio of galaxies to Galactic stars increases towards fainter magnitudes. The AGN fraction is put at $\sim$3% by Steidel et al. (2003, 2004). In the $G\mathcal{R}I$-selected $z\sim$4 sample, the foreground contamination is somewhat higher, $\sim$20%, although the statistics are fairly poor due to the small numbers of $G\mathcal{R}I$-selected objects with spectroscopy (Steidel et al. 1999).

In summary, the color-color selection criteria of Equations 4–7 select distinct populations with fairly narrow spreads in redshift of $\delta z\sim\pm$0.3 and with very little contamination by interlopers. We now turn to apply these well-understood selection criteria to our data.

4.2. *Our high-z galaxy sample*

The right-hand panel of Fig. 4 shows the $G-\mathcal{R}$ vs. $\mathcal{R}-I$ colors of the 23$\leq\mathcal{R}\leq$27 objects in the KDF. The right-hand panel of Figure 5 shows the U_n-G vs. $G-\mathcal{R}$ colors of 23$\leq\mathcal{R}\leq$27 objects, although — for clarity — only 1 in 3 objects are plotted. The color distributions of objects in these two figures are very similar to the corresponding brighter samples of the Steidel et al. surveys (see Fig. 2 of Steidel et al. 1999 and Fig. 1 of Steidel et al. 2003). This close similarity is not surprising given the similarity of the KDF image depths at $\mathcal{R}\sim$27 to theirs at $\mathcal{R}\sim$25.5. However, it does gives us strong reassurance that we are selecting identical populations, with similar photometric scatter, though at substantially fainter luminosities.

To $\mathcal{R}$=27.0, the color-color selection gives us 427 $z\sim$4, 1481 $z\sim$3, 2417 $z\sim$2.2, and 2043 $z\sim$1.7 star-forming galaxies in the 169 arcmin^2 of the KDF. This gives surface densities of, 2.5, 8.8, 14.3, and 12.1 arcmin^{-2} at $z\sim$4, $z\sim$3, $z\sim$2.2, and $z\sim$1.7, respectively. These densities are significantly higher than the surface densities of identically-selected but brighter objects in the $\mathcal{R}\leq$25.5 samples of Steidel et al. (1999, 2003, 2004), which is not surprising in light of the fact that the KDF probe considerably deeper into the faint end of the luminosity function at these redshifts. We discuss in detail the shape and evolution of the high-z galaxy luminosity function in a separate paper (Sawicki & Thompson, in prep.).

Figures 6–9 show the spatial positions of the color-color selected objects in our survey overplotted on the positions of all $\mathcal{R}$-selected objects. As with Fig. 2, there are detection "voids" in the vicinity of bright stars (c.f. Fig. 1). Additionally, however, the high-z galaxies shown in these four redshift slices do show significant real clustering: numerous voids and overdensities can be seen in all four redshift slices, and there are also hints of filaments, best seen in the $z\sim$4 sample in Fig. 6. High-z galaxies are, of course, well known to cluster, (e.g., Adelberger et al. 1998; Giavalisco et al. 1998; Ouchi et al. 2001), and their clustering can, for example, be used to constrain the properties of the dark matter halos that

they inhabit. Because of its depth, area, and large redshift span, our KDF sample is uniquely well suited to the study of clustering evolution and its dependence on luminosity. We will study these issues in detail in Sawicki & Thompson (in prep.).

4.3. Contamination and completeness of the high-z samples

As is the case in any color-color selection of high-z galaxies, our high-z samples may suffer both from selection bias and from contamination by foreground interlopers. Four effects can be at play: some high-z galaxies may be missed because they have *intrinsic* colors that are outside the color-color selection regions defined by Equations 4–7; low-z interlopers may be included because they have intrinsic colors inside the color-color selection regions; high-z galaxies with intrinsic colors that are inside the selection regions may scatter out of them due to photometric errors; and, finally, foreground interlopers may scatter into the selection regions due to photometric errors. These four effects will affect our completeness by making us miss some fraction of high-z galaxies from our sample, yet will also contaminate our sample with foreground interlopers. We discuss the importance of these four effects in turn, making particular use of the *spectroscopically constrained* contamination fractions of the Steidel et al. surveys.

1. *Low-z objects with intrinsic colors that place them in the high-z samples.* While the color-color selection criteria of Equations 4–7 are very effective at selecting high-z galaxies from the much more numerous foreground objects, they are not immune against low-z objects whose *intrinsic* colors place them in the high-z color-color selection boxes. The colors of certain types of Galactic stars, for example, put them into the regions of Equations 5–7, and the colors of $z\sim1$ red galaxies come dangerously close to the $z\sim4$ selection box defined by Equation 4 (see Steidel et al. 1999). Ordinarily, we would have no robust way of determining interloper fractions without recourse to *very* expensive spectroscopy. However, because we use the very same $U_nG\mathcal{R}I$ filters and color-color selection criteria as the Steidel group, we can use their spectroscopically-determined contamination fractions to constrain the fraction of such interlopers in our samples. At $\mathcal{R}\sim25$, the interloper fractions are $\lesssim5\%$ for $z\sim1.7$, 2.2, and 3, and $\sim20\%$ at $z\sim4$ (Steidel et al. 1999, 2003, 2004; see also § 4.1). Most of these interlopers are Galactic stars and intermediate-redshift ($z\sim1$) red galaxies. However, at the magnitudes of our survey, the interloper fractions should be lower than in the surveys of Steidel et al. because the ratio of galaxies to Galactic stars decreases at fainter magnitudes as one "punches" out of the Galaxy, and — similarly — the fraction of intermediate-z red galaxies decreases as one probes past the peak of their luminosity function. Thus, we can expect that the interloper fractions measured by Steidel et al. at $\mathcal{R}\sim25$ are *higher* than the interloper fractions at the fainter magnitudes of our survey. We therefore conservatively conclude that the interloper fractions in our $z\sim1.7$, 2.2, and 3 samples are $\lesssim5\%$, and are $\lesssim20\%$ at $z\sim4$.

2. *Low-z objects scattered into the high-z samples by photometric errors.* In addition to low-z interlopers whose *intrinsic* colors lie in the high-z color-color selection regions (effect #1 above), low-z interlopers with intrinsic colors *outside* the high-z selection criteria may get scattered into the selection regions by random photometric errors. The importance of such scatter could be crudely gauged using simulations. However, a more direct and robust approach is to note that the photometric errors of $\mathcal{R}\sim27$ objects in our imaging are similar to those of $\mathcal{R}\sim25.5$ objects in the Steidel et al. surveys. Because of this similarity we can expect expect similar interloper fractions in our survey as in theirs. The interloper fractions measured spectroscopically by Steidel et al. (1999, 2003, 2004) include *both* the photometrically-scattered interlopers being discussed here *and* the interlopers with intrinsic colors that place them in the high-z color-color selection regions (effect #1 above). We can therefore conclude that the sum of *both* classes of interlopers in our survey amounts to $\lesssim5\%$ at $z\sim1.7$, 2.2., and 3, and $\lesssim 20\%$ at $z\sim4$.

3. *High-z galaxies scattered out of the high-z samples due to photometric errors.* In addition to low-z objects being scattered by photometric errors into our color-color-selected samples (item #2 above), true high-z objects with intrinsic colors that should place them in these samples may be scattered out of the slection regions because of random photometric errors. To first order such scatter should be no larger than the scatter in the opposite direction (#2 above), given that the high-z galaxies are less numerous at a given apparent magnitude than low-z ones. However, the amount of such scatter can be gauged more accurately using Monte Carlo simulations and we will use such simulations as needed — for example when we use these data to study the high-z galaxy luminosity functions (Sawicki & Thompson 2004).

4. *High-z galaxies with intrinsic colors that place them outside our color-color selection criteria.* Finally, there exist high-z galaxies whose *intrinsic* colors lie outside the color-color selection regions defined by Equations 4–7. For example, sufficient amounts of interstellar dust will redden high-z galaxies out of our samples, moving them to the upper right in Figures 4 and 5. We have no way here to directly assess the size of such a missed population. We note, however, that our $U_nG\mathcal{R}I$ selection ensures that our fainter high-z samples misse *exactly the same* classes of high-z galaxies as are missed in the brighter work by the Steidel group. Therefore — unlike other optical LBG surveys that have to combine bright with faint samples selected using different filter sets and color-color selection criteria, we are free of *differential* bias in our sample selection. If we are biasing ourselves against certain classes of objects, we are doing so in the same way as the Steidel et al. samples, with no dependence on luminosity between our and their work.

Above we have discussed the ways in which objects may be scattered in and out of our high-z samples by photometric errors, and the ways in which our samples may be systematically contaminated and biased. We are greatly aided in determining our interloper fractions by our U_nGRI selection that is analogous to the Steidel et al. work. This identical selection is a key feature of our survey and confers upon us a great advantage over other deep surveys that use different selection criteria that have not been extensively tested and calibrated with spectroscopy.

5. SUMMARY AND DISCUSSION

In this paper we have introduced the Keck Deep Fields, a very deep U_nGRI imaging survey which we use to construct samples of very faint star-forming galaxies at $z\sim4$, $z\sim3$, $z\sim2.2$, and $z\sim1.7$. The key features of this survey are:

1. The KDF survey uses the very same U_nGRI filter set and spectroscopically-confirmed and -optimized color-color selection techniques developed by Steidel et al. (1999, 2003, 2004), thus obviating the need for expensive spectroscopic characterization of the sample and allowing us to confidently select *faint* star-forming galaxies at $z\sim4$, $z\sim3$, $z\sim2.2$, and $z\sim1.7$.

2. The completeness limit of the KDF is $\mathcal{R}_{lim}\sim27$ (with small field-to-field variations), where $\mathcal{R}_{lim}$ is the magnitude at which 50% of point sources are detected. Because optically-selected high-z galaxies are unresolved in our ground-based images, this magnitude limit is also the 50% completeness limit for high-z galaxies in our survey.

3. The KDF survey reaches up to ~1.5 magnitudes deeper than the wider-area, but shallower, imaging used by Steidel and collaborators, allowing us to select samples of much fainter, substantially sub-L^* objects at $z\sim4$, $z\sim3$, $z\sim2.2$, $z\sim1.7$ than are possible in the Steidel et al. surveys.

4. To $\mathcal{R}=27$, the KDF survey contains 427, 1481, 2417, and 2043, U_nGRI-selected star-forming galaxies at $z\sim4$, $z\sim3$, $z\sim2.2$, and $z\sim1.7$, respectively.

5. The KDF survey covers 169 arcmin^2 and is split into three widely-separated, spatially-independent patches on the sky. It thereby provides a large sample of high-z star-forming galaxies whose statistics are dominated neither by Poisson noise nor by cosmic variance.

Our survey complements directly the wider but shallower surveys by the Steidel team by extending their well-understood slection techniques to galaxies that are up to four times fainter than the limit of the Steidel et al. work. The depth and efficiency of the KDF stems from three factors: (1) In obvious contrast to the Steidel et al. surveys, which are typically carried out on 4m-class telescopes, our survey was undertaken on a much larger, 10m-aperture telescope; to first order, this simple increase in collecting area allows us to reach 6.25 times deeper per unit exposure time making our survey practical. (2) Additionally, we used a two-channel instrument, that allowed us to observe the same field in two wavebands simultaneously, thereby greatly decreasing the amount of total telescope time required. (3) Finally, in our second observing run — the run that yielded the bulk of our data — we benefited significantly from a very efficient, UV-optimized detector mosaic, that significantly reduced the necessary exposure times in G-, and — especially — U_n-bands.

In a great many respects, the KDF survey is the best currently available for the study of *faint* star-forming galaxies at $z\sim2$, 3 and 4. It holds very significant advantages over other very deep imaging surveys. For example, our survey is comparable in depth to the FORS Deep Field (FDF; Heidt et al. 2003), but covers ~3.5 times more area and is distributed over three spatially-independent patches compared to the FDF's single 48 arcmin^2 field. Our area is ~7 times smaller than the Subaru Deep Surveys 1200 arcmin^2 (SDS; Ouchi et al. 2004), but whereas the SXDF's $BVRi'$ filters allow the selection of only $z\sim4$ Lyman Break galaxies, our U_nGRI filter set lets us probe the ~2.2 Gyr time-span from $z\sim4$ to $z\sim1.7$; given our redshift coverage, we are in a position to study not just the properties but also the time evolution of the LBG population. The HST $UBVI$ imaging of the Hubble Deep Fields (HDFs; Williams et al. 1996, Casertano et al. 2002) matches ours in wavelength coverage and surpasses it in depth. However, the two HDFs combined cover a total of only ~10 arcmin^2, or a mere $\sim6\%$ of the area of our survey. Consequently, the HDFs are limited by Poisson noise in the number of objects and are more susceptible to the effects of large-scale structure. The Hubble Ultra Deep Field (UDF), deeper still than the HDFs, is similarly restricted to only a single small pointing, and, moreover, lacks deep U-band coverage, meaning that it is restricted to higher redshifts only. In addition to our advantages of area and/or wavelength coverage over *all* these surveys, one must also add the extremely important advantage that our survey gains from its use of the well-tested U_nGRI filter system. Our use of this filter system and its associated color-color selectios allows us to confidently select high-z galaxies and tie them *directly* to the work of the Steidel group at brighter fluxes.

To our knowledge, the only real competitor for the KDF survey is the GOODS project. The HST $BVIz$ imaging of the GOODS fields (Giavalisco et al. 2004), which covers twice the area of our survey and to a somewhat greater depth, provides an excellent dataset at $z\gtrsim4$. However, at $z\sim3$ and below, the lack of uniform U-band coverage of the GOODS fields makes them less useful since only the northern GOODS field has been imaged in U-band to a depth approaching that of our survey (~40 hrs in $\sim1.25''$ seeing with the KPNO 4m+Mosaic; Mauro Giavalisco, private communication). Thus, the GOODS U-band imaging covers an area nearly identical to that of our survey (160 arcmin^2 vs. our 169 arcmin^2) to a similar depth. However, this single GOODS field is potentially more affected by cosmic variance than is the sum of our three spatially independent patches. Moreover, as always, our KDF U_nGRI data holds the very significant advantage at all redshifts $z\approx2$–4 of being a *direct and straightforward* extension of the spectroscopically-

calibrated Steidel et al. selection technique. We therefore conclude that while the GOODS HST data dominates the field above $z=4$, the KDF are better suited for work at $z \lesssim 4$.

In the present paper — the first in a series — we have introduced our survey, described our observations and data reductions, and have shown our selection criteria for high-z star-forming galaxies. As we have argued above, in many ways ours is the best survey to study the population of *faint* star-forming galaxies from $z\sim4$ to $z\sim1.7$. The key features of our survey are its combination of depth with the well-understood $U_n G \mathcal{R}$ and $G \mathcal{R} I$ color-color selection.

With the survey introduced and the data described in the present paper, subsequent papers in this series will address in detail the properties and evolution of the population of very faint star-forming galaxies as the Universe ages by $2.5\times$ over the ~2.2 Gyr from $z\sim4$ to $z\sim1.7$.

REFERENCES

Adelberger, K.L., Steidel, C.C., Giavalisco, M., Dickinson, M.E., Pettini, M., & Kellog, M. 1998, ApJ, 505, 18

Bertin, E. & Arnouts, S. 1996, A&AS, 117, 393

Bolzonella, M., Miralles, J.-M., & Pelló, R. 2000, A&A, 363, 476-492

Bremmer, M.N., Lehnert, M.D., Waddington, I., Hardcastle, M.J., Boyce, P.J., & Phillipps, S. 2004, MNRAS, 347, L7

Brinchman, J. et al. 1998, ApJ, 499, 112

Casertano, S. et al. 2002, AJ, 120, 2747

Connolly, A.J., Csabai, I., Szalay, A.S., Koo, D.C., Kron, R.G., & Munn, J.A. 1995, AJ, 110, 2655

Csabai, I. et al. 2003, AJ, 125, 580

Erb, D.K., Shapley, A.E., Steidel, C.C., Pettini, M., Adelberger, K.L., Hunt, M.P., Moorwood, A.F.M., & Cuby, J.-G. 2003, ApJ, 591, 101

Giavalisco, M., Steidel, C.C., & Macchetto, F.D. 1996, ApJ, 470, 189

Giavalisco, M., Steidel, C.C., Adelberger, K.L., Dickinson, M.E., Pettini, M., & Kellog, M. 1998, ApJ, 503, 543

Giavalisco, M. et al. 2004, ApJ, 600, L93

Heidt, J. et al. 2003, A&A, 398, 49

Hogg, D.W., Pahre, M.A., McCarthy, J.K., Cohen, J.G., Blandford, R., Smail, I., & Soifer, B.T. 1997, MNRAS, 288, 404

Jenkins, A., Frenk, C.S., White, S.D.M., Colberg, J.M., Cole, S., Evrard, A.E., Couchman, H.M.P. Yoshida, N. 2001, MNRAS, 321, 372

Kron, R.G. 1980, ApJS, 43, 305

Lilly, S.J., Tresse, L., Hammer, F., Crampton, D., & Le Févre, O. 1995, ApJ, 455, 108

Lilly, S.J., Le Févre, O., Hammer, F., & Crampton, D. 1996, ApJ, 460, L1

McCarthy, J.K., et al. 1998, Proc. SPIE, 3355, 81

Metcalfe, N., Shanks, T., Campos, A., McCracken, H.J., & Fong, R. 2001, MNRAS, 323, 795

Oke, J.B. 1974, AJ, 27, 21

Oke, J.B., Cohen, J.G., Carr, M., Cromer, J., Dingizian, A., Harris, F.H., Labrecque, S., Lucinio, R., Schaal, W., Epps, H., & Miller, J. 1995, PASP, 107, 3750

Ouchi, M., et al. 2001, ApJ, 558, L83

Ouchi, M., et al. 2004, ApJ, 611, 660

Sawicki, M.J., Lin, H., & Yee, H.K.C. 1997, AJ, 113, 1

Sawicki, M. & Yee, H.K.C. 1998, AJ, 115, 1329

Sawicki, M. 2002, AJ, 124, 3050

Schade, D., Lilly, S.J., Crampton, D., Hammer, F., Le Févre, O., & Tresse, L. 1995, ApJ, 451, L1

Schlegel, D.J., Finkbeiner, D.P, & Davis, M. 1998, ApJ, 500, 525

Steidel, C.C., Giavalisco, M., Pettini, M., Dickinson, M., & Adelberger, K.L. 1996, ApJ, 462, L17

Steidel, C.C., Adelberger, K.L., Giavalisco, M., Dickinson, M., & Pettini, M. 1999, ApJ, 519, 1

Steidel, C.C., Adelberger, K.L., Shapley, A.E., Pettini, M., Dickinson, M., & Giavalisco, M. 2003, ApJ, 592, 728

Steidel, C.C., Shapley, A.E., Pettini, M., Adelberger, K.L., Erb, D.K., Reddy, N.A., & Hunt, M.P 2004, ApJ, 604, 534

Vogt, N. et al. 1997, ApJ, 479, L121
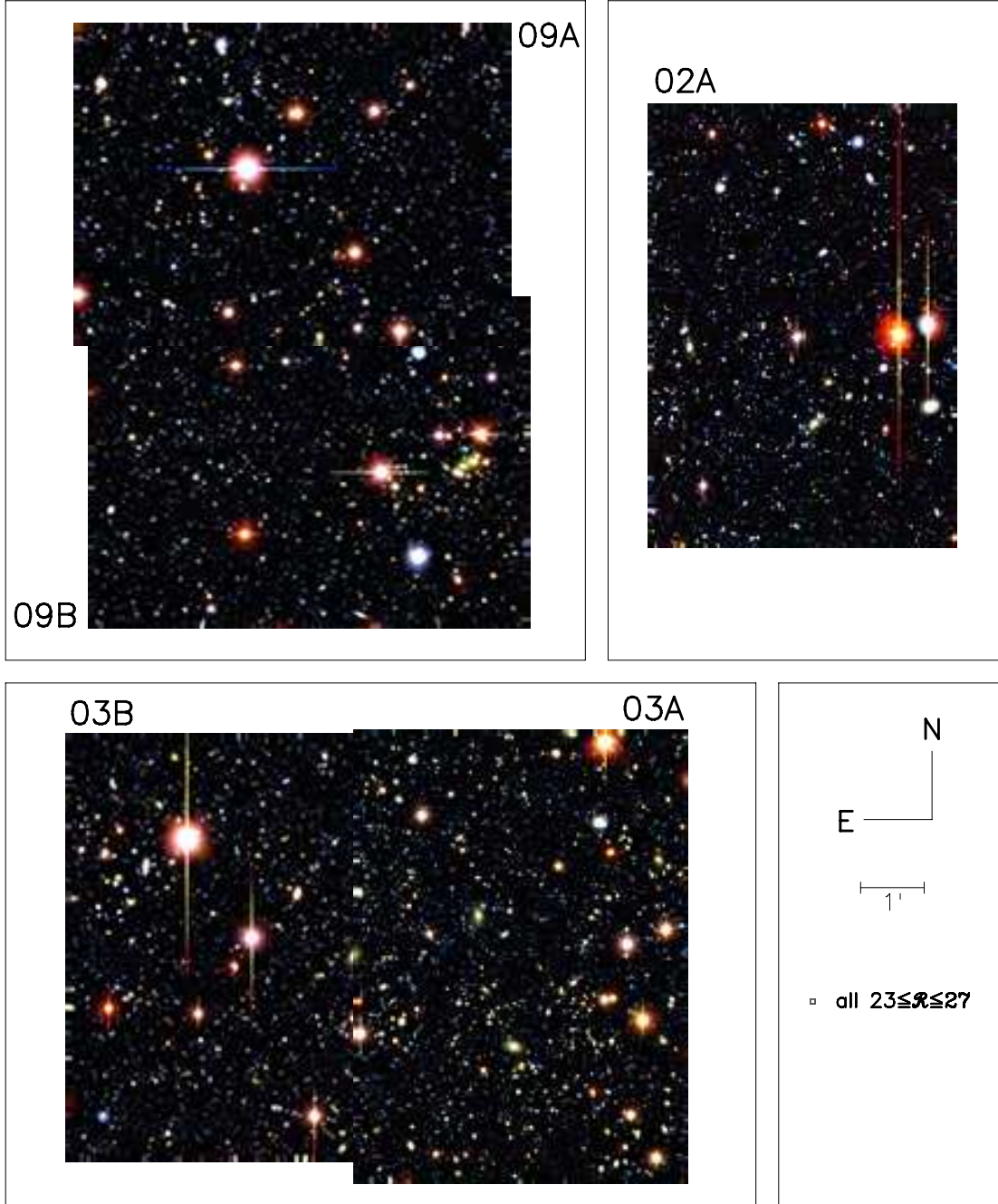
Williams, R.J., et al. 1996, AJ, 112, 1335

Sawicki & Thompson

FIG. 1.— A HIGH RESOLUTION VERSION OF FIGURE 1 CAN BE OBTAINED FROM THE AUTHORS. Composite $G\mathcal{R}I$ color images of the KDF. I-band is shown as red, $\mathcal{R}$-band as green, and G-band as blue. Although we have made a reasonable attempt at colormap consistency between the fields, small systematic color differences between the fields in this figure may remain. Therefore, apparent differences between colors of objects from field to field in this figure should not be overinterpreted.
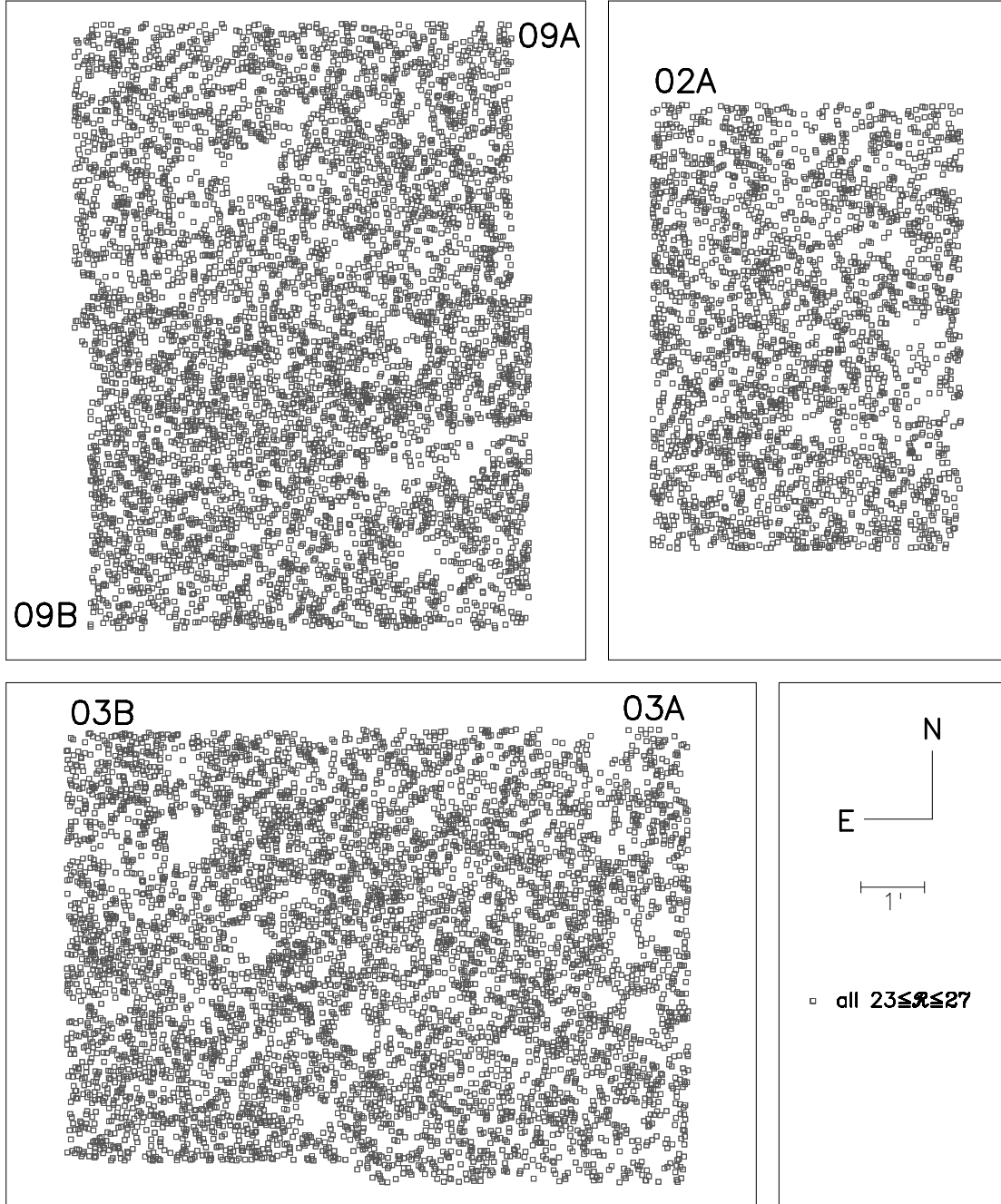
FIG. 2.— Positions of all objects with 23<$\mathcal{R}$<27. Note "holes" in which object-finding was affected by light from bright foreground objects.
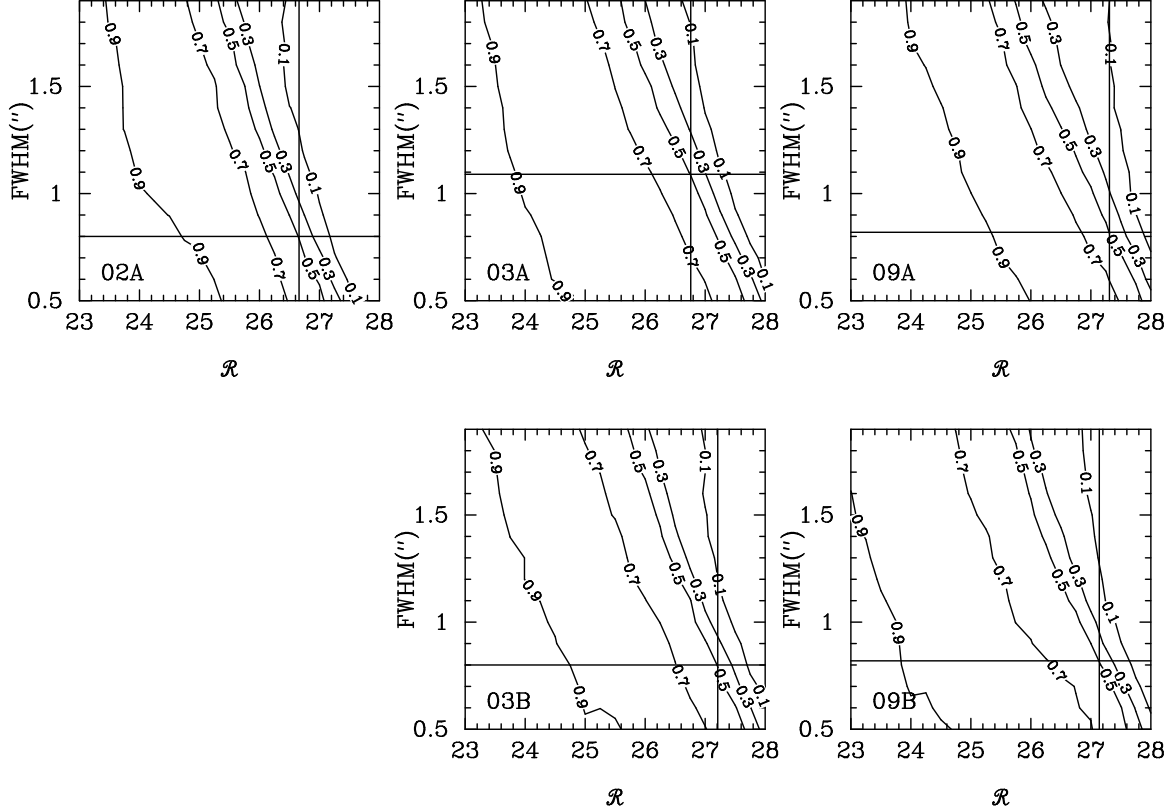
FIG. 3.— Completeness as a function of $\mathcal{R}$ magnitude and object size. Contours show completeness deremined from simulations (see text). Object compactness is parametrized as Gaussian FWHM — as is appropriate for intrinsically compact objects that are unresolved in our ground-based images. The point-source FWHM values are shown as horizontal lines. High-z star-forming galaxies are compact and virtually unresolved under the $\geq 0.8''$ seeing in these images and therefore their sizes are well approximated by the horizontal lines. Our limiting magnitudes, $\mathcal{R}_{lim}$, are defined as the magnitudes that correspond to 50% detection efficiency for unresolved objects. They are $\mathcal{R}_{lim} \sim 27$ and are shown with vertical lines.
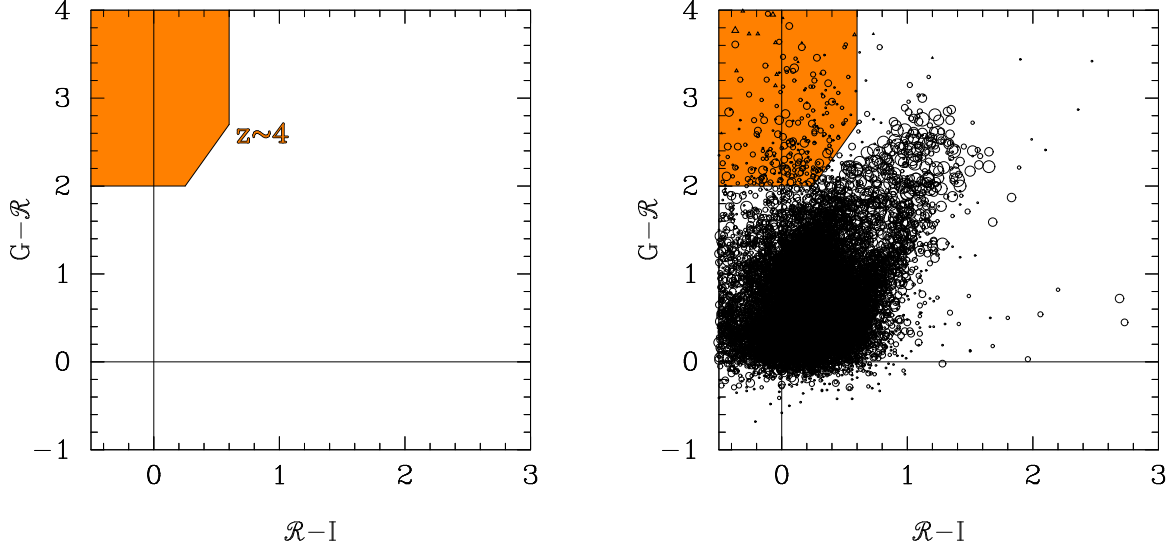

FIG. 4.— $G\mathcal{R}I$ color-color plots. The redshift selection region defined by Equation 4 is highlighted in orange; the filters and color-color selection used are identical to those used by Steidel et al. (1999) to select $z \sim 4$ galaxies. The colors of objects with $23 \leq \mathcal{R} \leq 27$ are shown in the right-hand panel. Circles denote objects that were significantly detected in all bands, and upward-pointing triangles show objects with G-band upper flux limits only. Symbol size corresponds to $\mathcal{R}$ magnitude. Note the close similarity of the color-color distribution in this figure to that in, e.g., Fig. 2 of Steidel et al. (1999).
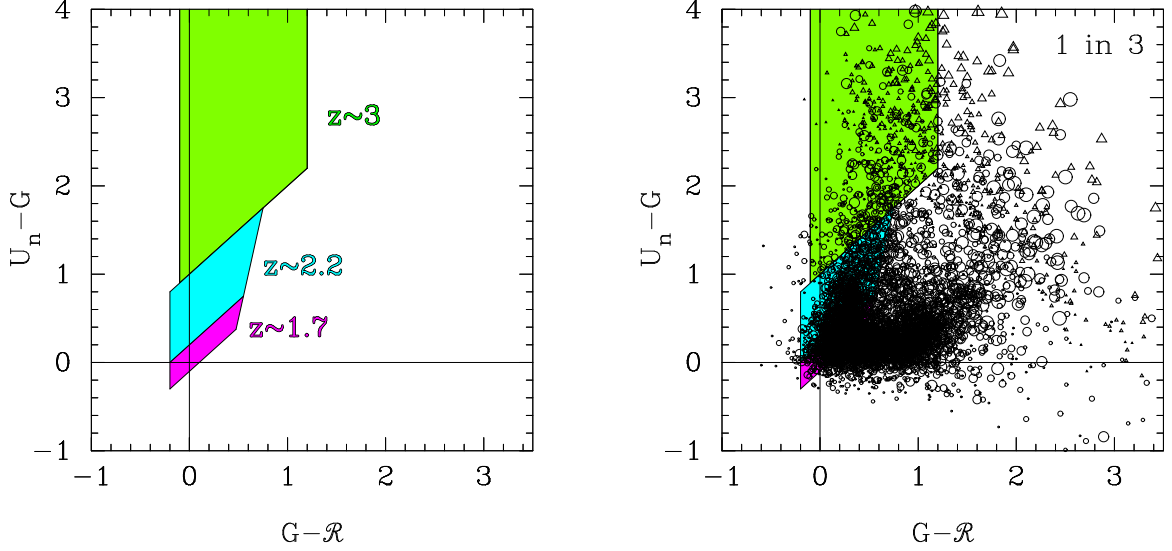
FIG. 5.— $U_nG\mathcal{R}$ color-color plots. The left panel shows redshift selection regions defined by equations 5 (green), 6 (blue), and 7 (magenta). These regions are *identical* to the well-known and well-characterized selection criteria of Steidel et al. (2003, 2004). The right panel shows the colors of our objects with $23 \leq \mathcal{R} \leq 27$. For clarity, only one object out of three is plotted. Circles denote objects that were significantly detected in all bands, and upward-pointing triangles show ubjects with U_n-band upper limits only. Symbol size corresponds to $\mathcal{R}$ magnitude. Note the close similarity of the color-color distribution of objects in this figure to that in, e.g., Fig. 1 of Steidel et al. (2004).

TABLE 1. FIELD DETAILS

	02A	03A	03B	09A	09B
RA (2000)[a]	02:09:41.3	03:21:38.6	03:21:57.6	09:33:36.9	09:33:35.8
Dec (2000)[a]	−04:37:46	−04:19:19	−04:19:10	+28:48:19	+28:43:58
size[b]	7.00′×4.93′	7.15′×5.26′	6.75′×4.81′	6.89′×5.07′	6.92′×5.24′
$E(B-V)$[c]	0.024	0.031	0.031	0.018	0.018
$t_{exp}(U_n)$[d]	9600s [e]	21600s [f]	14400s [e]	22800s [f]	18000s [e]
$t_{exp}(G)$[d]	7200s [e]	9600s [e]	10800s [e]	12000s [f]	10800s [e]
$t_{exp}(\mathcal{R})$[d]	6300s [g]	21870s [g]	13125s [g]	25335s [g]	12075s [g]
$t_{exp}(I)$[d]	3575s [g]	9720s [g]	10100s [g]	10440s [g]	6500s [g]
seeing (U_n)[h]	0.98″	1.38″	0.93″	1.03″	0.97″
seeing (G)[h]	0.99″	0.78″	0.83″	1.10″	1.05″
seeing $(\mathcal{R})$[h]	0.80″	1.09″	0.80″	0.82″	0.82″
seeing (I)[h]	0.89″	1.30″	1.00″	0.93″	0.88″
common smoothed seeing[i]	1.0″	1.4″	1.0″	1.1″	1.1″
$\mu_{lim}(U_n)$[j]	30.4	30.4	30.7	31.0	30.6
$\mu_{lim}(G)$[j]	30.5	30.6	31.0	30.8	30.8
$\mu_{lim}(\mathcal{R})$[j]	29.3	30.1	29.9	30.0	29.9
$\mu_{lim}(I)$[j]	28.7	29.3	29.3	29.5	29.5
$\mathcal{R}_{lim}$[k]	26.66	26.76	27.21	27.31	27.14
N($22.5 \leq \mathcal{R} \leq 25.0$)[l]	30.3	29.0	30.1	22.6	26.6

[a]Approximate coordinates of the field center
[b]Includes regions of overlap between 03A and 03B, and 09A and 09B
[c]Foreground dust attenuation in Schlegel et al. (1998) maps
[d]Exposure time in the final, stacked image
[e]Taken with the UV-optimized EEV CCD mosaic
[f]Taken with the blue-side engineering-grade SITe CCD
[g]Taken with the SITe/Tektronix 2k×2k CCD
[h]Median of a number of unsaturated point sources
[i]Seeing in the final, stacked and smoothed images
[j]1σ surface brightness limit in mag/arcsec^2
[k]Magnitude at which 50% of point sources are detected in the stacked (but not smoothed) image
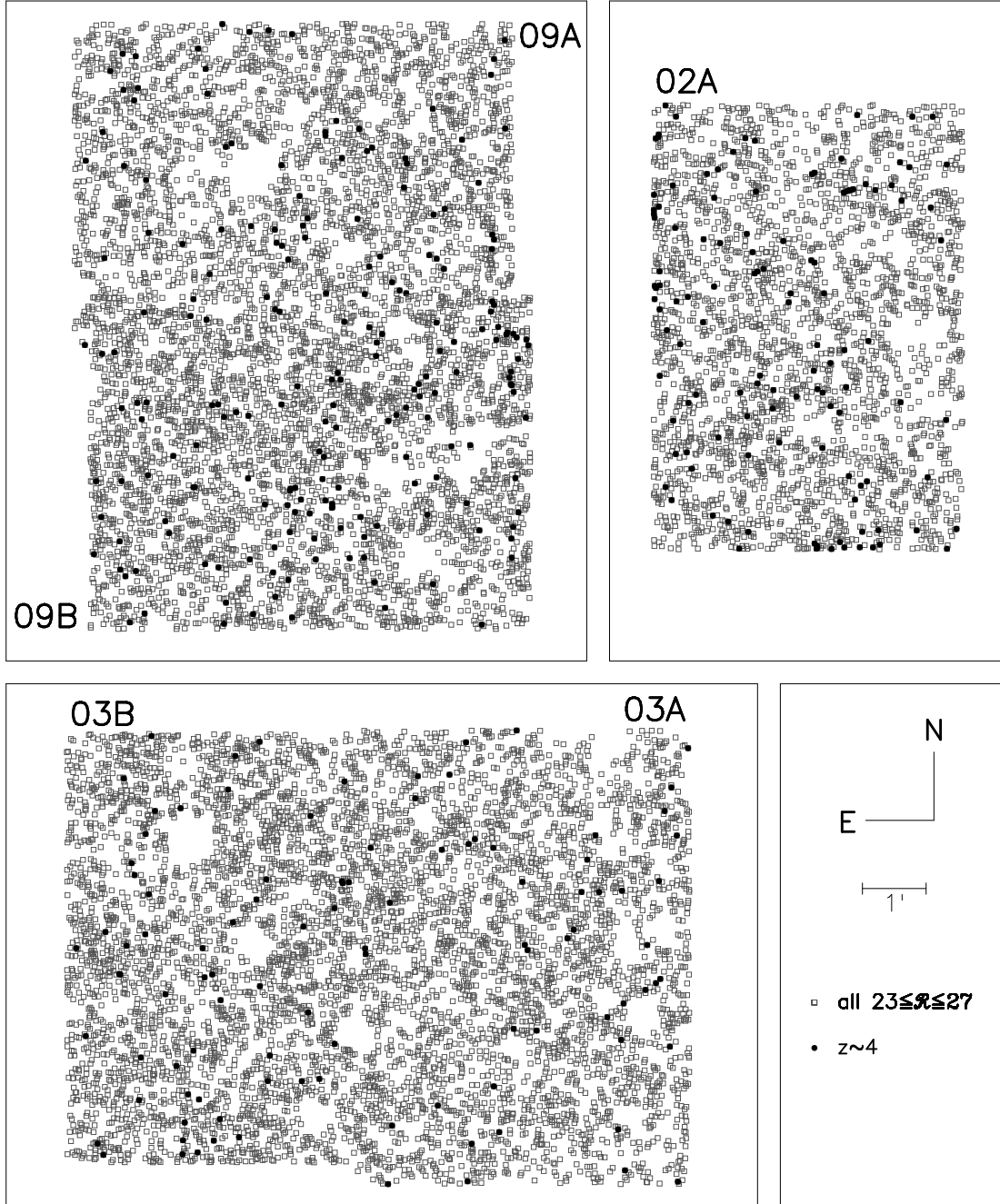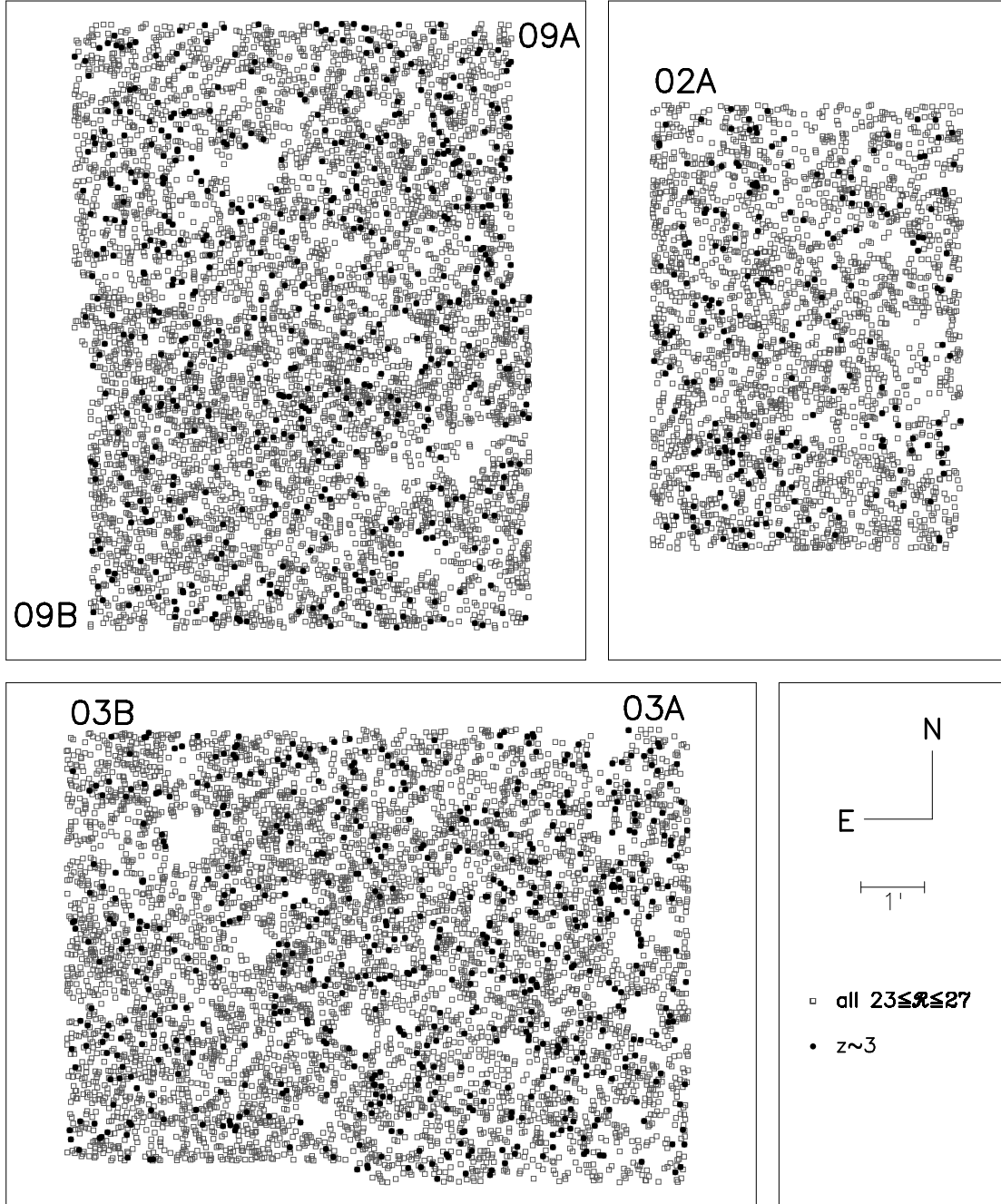[l]Number of objects per arcmin^2 detected in the magnitude range $\mathcal{R}$=22.5–25.0

FIG. 6.— Positions of $z\sim4$ color-selected star-forming galaxies overplotted on top of the positions of all $23\leq\mathcal{R}\leq27$ objects in the survey.

Fig. 7.— Positions of $z\sim3$ color-selected star-forming galaxies.
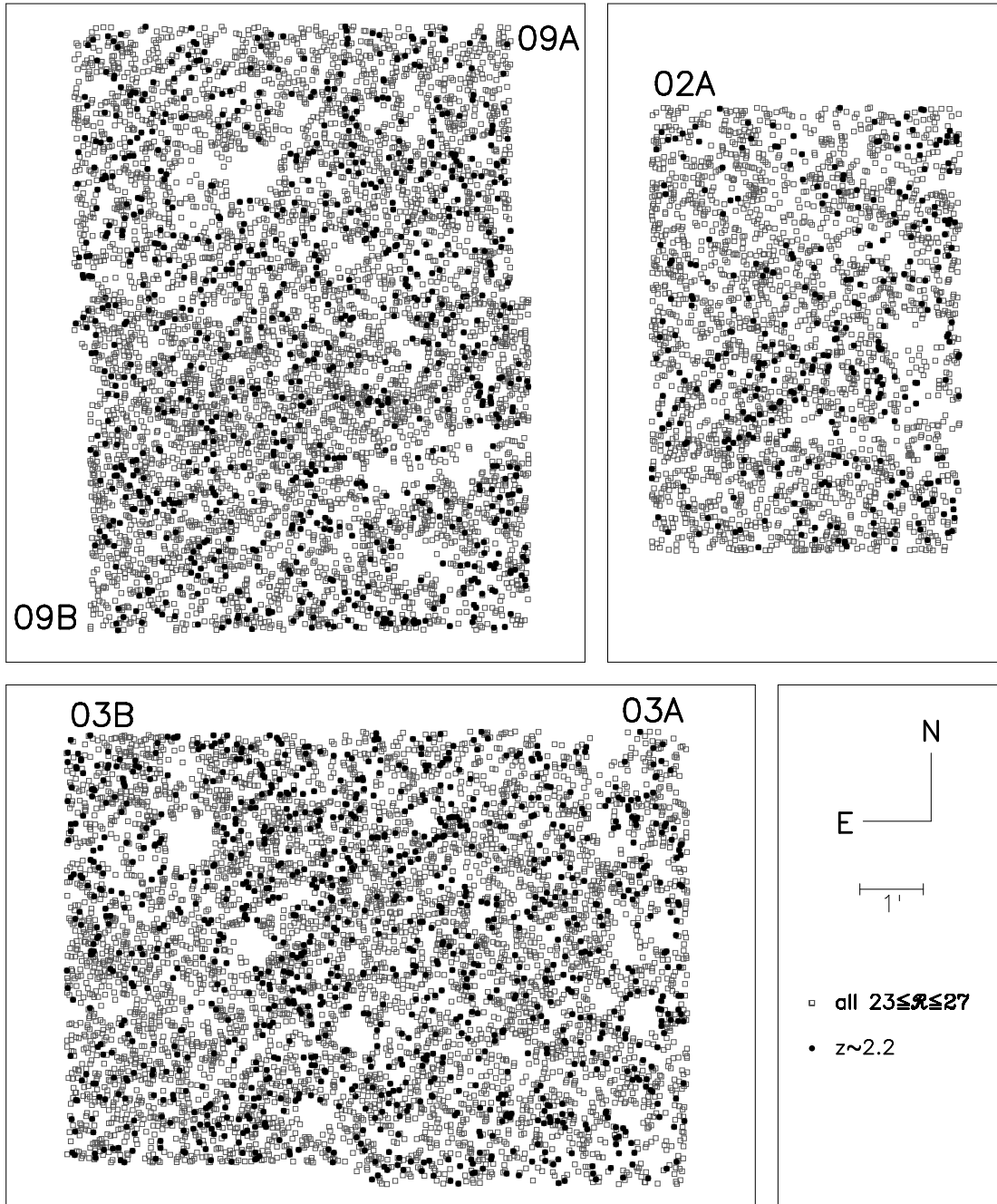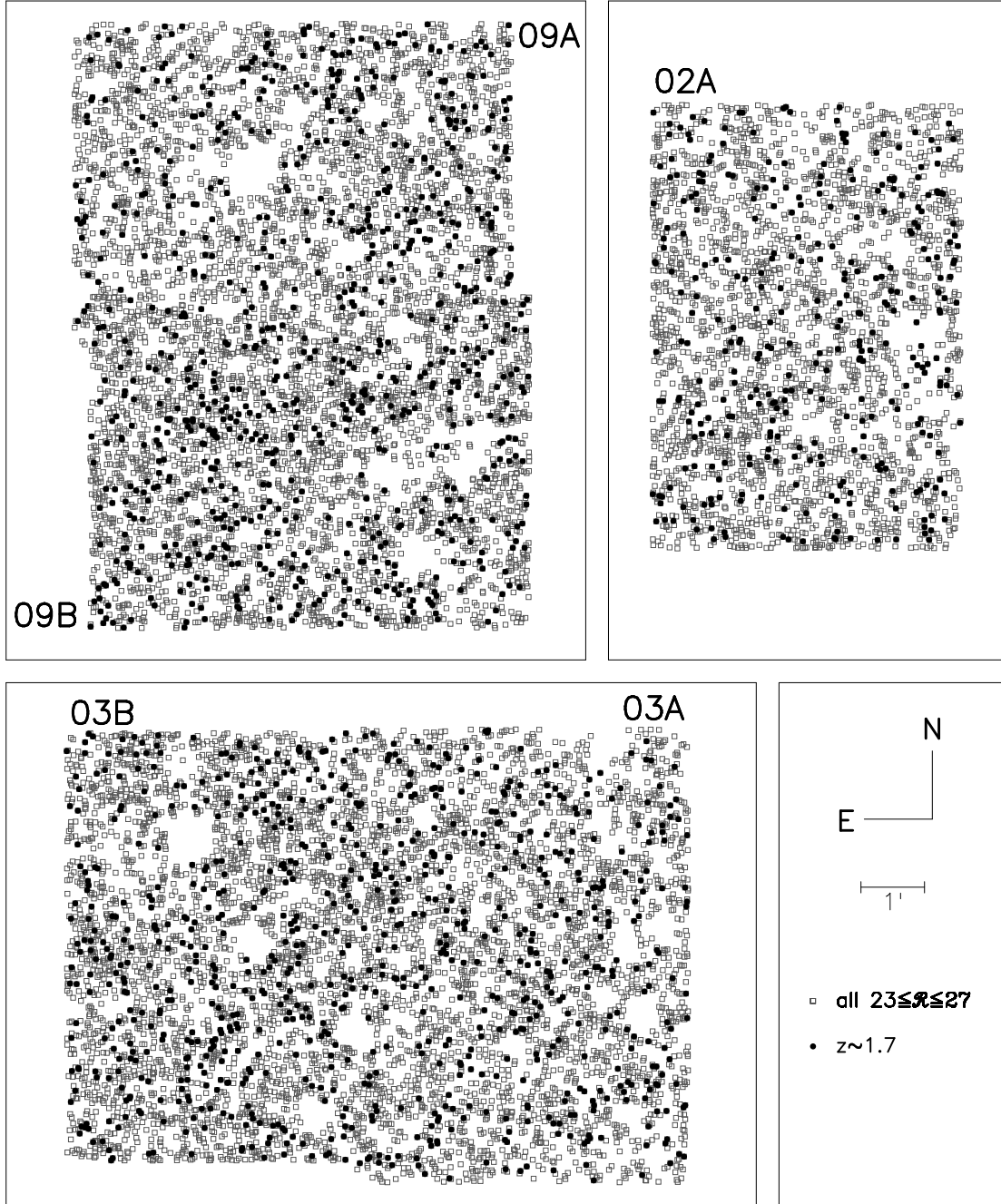
Sawicki & Thompson

FIG. 8.— Positions of $z\sim2.2$ color-selected star-forming galaxies.

Fig. 9.— Positions of $z \sim 1.7$ color-selected star-forming galaxies.